International Journal of Hydrogen Energy 168 (2025) 150939

Contents lists available at ScienceDirect

International Journal of Hydrogen Energy

journal homepage: www.elsevier.com/locate/he

Development of a nickel-based catalyst for syngas production via tri-reforming of biogas

Andrea Brigliadori [a], Filippo Suzzi [a], Andrea Bartoletti [a], Elisa Mercadelli [a], Davide Gardini [a], Elisabetta Orfei [b], Andrea Fasolini [b], Jacopo De Maron [b], Francesco Basile [b,*], Angela Gondolini [a,**], Alessandra Sanson [a]

[a] CNR-ISSMC, Institute of Science, Technology and Sustainability for Ceramics National Research Council of Italy, Via Granarolo, 64, Faenza, 48018, Italy
[b] Department of Industrial Chemistry, C3-Centre for Chemical Catalysis, CIRI-FRAME Alma Mater Studiorum – University of Bologna, Viale Risorgimento 4, 40136, Bologna, Italy

ARTICLE INFO

Handling Editor: Dr M Djukic

Keywords:
Biomass valorization
Tri-reforming
Metal foam
LDH
Dip-coating

ABSTRACT

Thermo-chemical biomass valorization processes, such as tri-reforming, constitute a valid renewable alternative to produce chemicals, fuels, and energy. In this work, a structured Ni-based catalyst for biogas tri-reforming was developed for the first time by coupling a Ni/Mg/Al oxide active phase with a commercial Ni/Cr/Al-based metal foam support. The active phase was obtained by calcinating the layered double hydroxides (LDHs) precursor prepared via chemical synthesis and the catalyst was assembled by dip-coating. For this purpose, a stable aqueous suspension capable of dispersing the active phase and ensuring a homogeneous substrate covering was thoroughly optimized. The stability of the catalyst exposed to the reaction environment was evaluated by FE-SEM/EDX, confirming the durability of the coating. The Ni-based structured catalyst demonstrated promising performances, ensuring a stable CH_4 conversion of 97.7 % and only a slight reduction of CO_2 conversion after more than 17 h, with a syngas productivity >9500 mL•min^{-1}•g^{-1}.

1. Introduction

In recent years, the increasingly important issues related to climate change, global warming, and the depletion of available resources have forced the scientific community's attention towards new energy efficiency solutions. Within this scene, the exploitation of renewable energy sources, such as solar, wind, hydraulics, and biomass, is fundamental from a circular economy perspective. Biomass can play a key role in reducing the carbon footprint: by giving new life to waste derived from agriculture, animals, plants, and industrial and urban activities is possible to obtain new bio-chemicals, bio-fuels, and green energy [1].

Among the various processes for converting and exploiting biomass, thermo-chemical processes are extensively studied, with pyrolysis and gasification being the most relevant. Pyrolysis occurs in an inert environment at medium (300–800 °C) or high (800–1300 °C) temperatures to convert biomass into products with higher energy density, such as bio-char, bio-fuels, bio-oils, or syngas. Gasification is focused on producing syngas, a mixture of gaseous components mainly consisting of H_2 and CO, with secondary fractions of CO_2, CH_4, H_2S, NH_3, light and heavy hydrocarbons, and further impurities such as ash and tar [1–3].

The optimization of the gasification process to maximize H_2 and CO yield has led to the development of tri-reforming of methane (TRM). TRM is based on the coupling of three reactions: steam reforming (Eq. (1)), dry reforming (Eq. (2)), and partial oxidation (Eq. (3)). This combination allows working in autothermal conditions and avoiding external heating sources, which could involve potential CO_2 emissions [4].

$$CH_4 + H_2O \rightarrow CO + 3H_2 \left(\Delta H^0_{25\,^\circ C} = 206\ kJ \cdot mol^{-1}\right) \quad \text{(Eq. 1)}$$

$$CH_4 + CO_2 \rightarrow 2CO + 2H_2 \left(\Delta H^0_{25\,^\circ C} = 247\ kJ \cdot mol^{-1}\right) \quad \text{(Eq. 2)}$$

$$CH_4 + \frac{1}{2}O_2 \rightarrow CO + 2H_2 \left(\Delta H^0_{25\,^\circ C} = -38\ kJ \cdot mol^{-1}\right) \quad \text{(Eq. 3)}$$

As dry reforming can be considered the combination of Reverse Water Gas Shift (reverse WGS) and steam reforming, another reaction

* Corresponding author.
** Corresponding author.
E-mail addresses: f.basile@unibo.it (F. Basile), angela.gondolini@issmc.cnr.it (A. Gondolini).

https://doi.org/10.1016/j.ijhydene.2025.150939
Received 18 April 2025; Received in revised form 7 July 2025; Accepted 9 August 2025
Available online 21 August 2025

can be considered (Eq. (4)).

$$CO_2 + H_2 \rightarrow CO + H_2O \left(\Delta H^0_{25\,^\circ C} = 41\ kJ \cdot mol^{-1}\right) \quad \text{(Eq. 4)}$$

This reaction is driven by the equilibrium conditions and highly influenced by the exit temperature of the catalytic bed [5].

Generally, TRM catalysts can be grouped into two categories: noble metals and non-noble metals [6–10]. Noble metals are highly active and more resilient against fouling. In contrast, non-noble transition metals such as nickel- or cobalt-based catalysts demonstrated comparable activity to noble metal-based catalysts but faster deactivation. Recently, nickel-based catalysts have been widely used in the TRM process for syngas production [11,12]. This is because nickel nanophases have shown good activity and selectivity toward methane-reforming reactions [13]. The main challenges of these catalysts are deactivation and fouling. To address these problems, the development of new 3D catalytic systems [14,15] has aimed at stabilizing nickel nanophases on suitable substrates, typically single or mixed metal oxides such as Al_2O_3, CeO_2, ZrO_2, TiO_2, and MgO [12]. Moreover, TRM is typically conducted in fixed or fluidized bed reactors using pellets of the catalytic material, which presents several critical issues, including heat transfer limitations, deactivation, poisoning, and mechanical instability, leading to the release of dust and residues [16]. To minimize these problems, more complex catalysts have been developed by dispersing nickel-based active phases on different substrates, such as La_2O_3-αAl_2O_3 [13], FeCrAl monolith [16], MOF-derived ZrO_2 [17], or hydroxyapatite [18] aiming to obtain a finer dispersion of nickel nanophases. Furthermore, the use of structured/monolithic catalysts presents several advantages with respect to the conventional pellets, including an improved thermal conduction along the reactor and therefore a flatter thermal profile [19]. In this way, cold zones at the end of the catalytic bed can be avoided due to the occurrence of endothermic reactions, thus reducing activity losses and deactivation caused by the production of H_2S, which is favoured at low temperatures. Ceramic and metallic foams are well-known substrates used for a long time as filters or membranes, and more recently, they have been applied in catalysis as supports for the active phases. Metallic foams offer good mechanical properties and better thermal and electrical conductivity, while ceramic foams provide better resistance to high temperatures and harsh chemical environments. Several materials were used to produce foams to be wash-coated for catalytic applications, e.g. Al_2O_3, ZrO_2, SiC, Al, Ni, Cu, steel, stainless steel, FeCrAlY, and zeolite [20]. Porous metallic foams impregnated with the desired active phase could be an interesting solution to improve the gas flow and the thermal conduction through the catalyst. In this context, the dip-coating represents an easy, scalable, and economical technique commonly used also for the preparation of gas separation membranes and solid oxide cell components, or the impregnation of catalytic phases over electrodes [21,22]. Moreover, it is suitable for the controlled deposition of a thin layer of active phase over differently shaped and with large surface supports. Varying the physicochemical properties of the dip-coating suspension and controlling the process parameters, such as immersion time and withdrawal speed, the homogeneity and thickness of the coating layer can be properly tuned [21–23].

Recently, several authors reported the production of structured catalysts for thermo-chemical processes using metallic foams. Prioriello et al. deposited by the wash-coating method a Ru-loaded $CaZr_{0.85}Sm_{0.15}O_{3-\delta}$ perovskite oxide on a NiCrAl foam for the Indirect Internal Reforming (IIR) of biogas in Solid Oxide Fuel Cell (SOFC) [24]. Santoro et al. prepared a structured catalyst for the dry reforming of methane, depositing a nickel-based samarium-doped ceria (Ni-SmDC) phase via wash-coating on a NiCrAl foam [25]. Basile et al. electro-deposited Rh/Mg/Al hydrotalcite syngas catalyst precursor on the surface of FeCrAlloy foam to study the catalytic partial oxidation of methane to syngas [26–30]. Varvoutis et al. produced a catalyst for the CO_2 methanation; they wash-coated Ni/CeO_2 nanorods on a highly porous NZP-type ceramic substrate of $Ba_{1+x}Zr_4P_{6-2x}Si_{2x}O_{24}$ [31]. The main advantages reported in the literature using these types of structured catalysts are the improved thermal control and reduction of hot spots with consequent fouling reduction, lower pressure drops, and high catalytic activity due to the efficient dispersion of the active phase. However, the primary drawbacks of coated foam catalysts remain the limited understanding of transport processes in irregular structures and the potential peeling of the coating in the reaction environment due to differential thermal stresses [20].

Despite the growing interest in Ni-based catalysts derived from layered double hydroxides (LDHs), their potential applications remain largely unexplored in the literature. To the best of our knowledge, only a few studies have investigated such catalysts for TRM. Kumar et al. examined hydrotalcite-derived Mg–Al mixed oxide-supported Ni catalysts, assessing the promotional effects of Cu and Zn under reaction conditions of 800 °C, 1 atm, SV 49200 mL h^{-1} g^{-1}, and a molar feed composition of CH_4:CO_2:H_2O:O_2:N_2 = 1:0.23:0.46:0.07:0.28 [32]. Their best performance was achieved using a Ni–Mg–Al catalyst calcined at 900 °C, with CH_4 and CO_2 conversions of 64 % and 75 %, respectively [32]. Similarly, Da Costa et al. explored Ni/Mg/Al hydrotalcite-derived catalysts under different reaction conditions, obtaining the highest average CH_4 and CO_2 conversions (98.2 % and 69.3 %, respectively) at a feed composition of CH_4:CO_2:H_2O:O_2/Ar = 1/0.5/0.5/0.1/7.9, GHSV of 20000 h^{-1}, and a temperature range of 600–850 °C [33]. However, structured catalysts for this process have not yet been extensively studied. In particular, metal foams remain untested, though Solov'ev et al. reported the use of synthetic cordierite in the form of honeycomb-structured blocks (cell size 1 × 1 mm, wall thickness 0.2 mm) as a structured support for Ni-based catalysts [34]. Among the different process parameters and catalyst formulations investigated, they achieved the best performance (CH_4 conversion: 99 %, CO_2 conversion: 43 %) using a NiCeAl-based catalyst at 705 °C with a gas feed composition of CH_4:CO_2:H_2O:O_2/Ar = 1/0.7/0.2/0.65/14.5 [34]. As reported in the literature, ceramic oxide foams used as catalytic supports exhibit limited thermal conductivity. Depending on the specific material, porosity type, and pore density, thermal conductivity values for commonly used ceramic oxides such as Al_2O_3, TiO_2, and SiO_2 have been observed to range from 0.027 to 0.160 W m^{-1} K^{-1} [35,36]. NiCrAl metal foam has demonstrated superior oxidation resistance at high temperatures compared to NiCr alloy. Additionally, NiCrAl foam exhibits higher thermal conductivity than FeCrAl, with reported values of 0.257 and 0.098 W m^{-1} K^{-1}, respectively [37]. The combination of high thermal conductivity, good oxidation resistance and mechanical strength makes NiCrAl metal foam an attractive material for use as support for structured catalysts, enabling improved thermal control along the catalytic bed.

In this work, a commercial NiCrAl metal foam was coupled with NiMgAl active phase, exploiting the affinity of the two phases to develop an active, efficient, and resistant catalyst. The nickel-based catalyst for TRM supported on the NiCrAl foam was produced for the first time via dip-coating. The active phase catalyst was synthesized by co-precipitation of a layered double hydroxides (LDH) phase consisting of Ni, Mg, and Al, subsequently calcined to obtain mixed oxides. The resulting powder was used for the optimization of the suspension to be deposited via dip-coating. Several deflocculants, binders, and surfactants were employed to develop a stable water-based suspension with rheological properties suitable for the dip-coating process. The deposition conditions and thermal treatments were adjusted to create a homogenous layer of active phase. The catalyst developed in this study was tested in the TRM, obtaining excellent results in terms of CH_4 conversion (97.7 %), CO_2 conversion (80 %), and syngas productivity (>9500 mL•min^{-1}•g^{-1}). The catalyst demonstrated very good durability, showing high activity after repeated testing cycles and preserving the homogenous structure of the coating with no sign of detachment or peeling off.

2. Experimental

2.1. Synthesis of the Ni/mg/al mixed oxides active phase

The active phase is constituted by Ni, Mg, and Al mixed oxides, whose synthesis has been described elsewhere [38]. Briefly, Ni/Mg/Al layered double hydroxides (LDH) precursor was synthesized by an optimized coprecipitation technique [39–41], starting from nitrates. Ni $(NO_3)_2$•$6H_2O$ (99 %, Sigma-Aldrich), $Mg(NO_3)_2$•$6H_2O$ (99 % Sigma-Aldrich), and $Al(NO_3)_3$•$9H_2O$ (99 % Sigma-Aldrich) were dissolved in water with the following stoichiometry $Ni_{24}Mg_{56}Al_{20}$, to have a M^{2+}/M^{3+} molar ratio of 4, with a total cations concentration of 2.0 M. These solutions were slowly added to 1.0 M Na_2CO_3 at 60 °C, kept at a constant pH of 10.0 ± 0.5 by the addition of 3.0 M NaOH. The final suspension was stirred for 45 min at 60 °C, then the solid was filtered, washed with 2 L of deionized water, and dried for 18 h at 70 °C. The material was ground, and the obtained LDH powder was calcined at 650 °C for 12 h with a heating ramp of 10 °C•min^{-1} to obtain the corresponding $Ni_{24}Mg_{56}Al_{20}$ mixed oxide phase.

2.2. Preparation of the catalyst: optimization of the suspension and dip-coating deposition

The catalyst was prepared via dip-coating, using, as support, a commercial NiCrAl metallic foam (Alantum Europe GmbH) with 450 μm average pore size (≈90 vol% porosity), previously treated at 1150 °C for 30 min (Ar+1 %O_2). These oxidizing conditions were optimized to develop an Al_2O_3 surface layer [42]. To perform the deposition of a thin layer of $Ni_{24}Mg_{56}Al_{20}$ mixed oxide, an in-depth study was carried out to optimize the suspension. Both as-synthesized and milled powders were used to prepare the suspensions. The former was dispersed by combining the simultaneous action of a 20 kHz sonication probe (VCX 500 Ultrasonic Microprocessor, Sonics Materials; 10 s sonication + 2 s rest, for a total time of 18 min, corresponding to a power delivered of 28 W) and magnetic stirring.

Whereas the milled powder was treated by a high-energy planetary ball-milling (Pulverisette 6, Fritsch) using a zirconium dioxide jar and beads to reduce the particle size and increase the suspension's stability, 30 consecutive milling cycles (10 min, 400 rpm co-rotation + 10 min rest) were carried out. Dip-coating was performed using a custom-made dip-coater manufactured by Aurel S.p.A., suitable for the depositions from laboratory to pre-industrial scale. Depositions were conducted using 6 x 5 × 1.6 cm^3 NiCrAl substrates with an immersion and withdrawal speed of 0.1 mm•s^{-1}, and a residence time of 300 s. The coating was dried at 120 °C for 30 min, and the samples were subsequently calcined at 900 °C for 1 h to burn out the organics and oxidize the active phase. Repeated dip-coating cycles (from 1 to 4) were performed to achieve a homogeneous coating.

2.3. Powder, suspension and catalyst characterization

The mixed oxide powder was dispersed in water and a combined particle size analysis was carried out by dynamic light scattering (DLS) to measure the hydrodynamic diameter of the colloidal fraction (Zetasizer Nano ZSP, Malvern Panalytical) and by gravitational sedimentography to assess the diameter of the micrometric fraction (SediGraph III Plus, Micrometrics). The zeta potential of the suspension was studied by electrophoretic light scattering (ELS); the instrument (Zetasizer Nano ZSP, Malvern Panalytical) equipped with an automatic titrator (MPT-2) allowed also the titration of the zeta potential as a function of the pH (0.1 M HCl and 0.1 M KOH were used as titrants) and the titration of the zeta potential as function of the deflocculating agent's concentration. Darvan 821-A (Vanderbilt Minerals), Dolapix CA (Zschimmer & Schwarz), and Dolapix PC 21 (Zschimmer & Schwarz) were tested as deflocculants to improve the suspension's stability.

The rheological properties of the suspensions were evaluated using a controlled stress rotational rheometer (C-VOR 120, Bohlin Instruments) equipped with a double gap coaxial cylinder geometry (DG40/50). Viscosity at 20 °C has been monitored within the shear rate range 10^{-1}-10^3 s^{-1}. Hydroxypropyl cellulose (HPC, 99 %, Alfa Aesar, MW 100000 g•mol^{-1}) and polyvinyl alcohol (PVA, 99 %, Sigma-Aldrich, MW 30000–70000 g•mol^{-1}, 87–90 % hydrolyzed groups) were used as binders to increase the suspension's viscosity while improving the stability and dispersion of the powders.

Contact angle measurements were performed using a drop shape analyzer DSA 30S (Krüss GmbH) with a sessile drop method. The wettability of the commercial foam with the powder suspension was enhanced by introducing a surfactant (Surfynol SE-F, Air Products) to improve the coating deposition.

Powders and coated foams were observed by field emission-scanning electron microscopy (FE-SEM, Carl Zeiss Sigma), mounting an energy dispersive X-ray spectroscopy probe (EDX, micro-analysis system device Oxford Energy X-Act) for the elemental analysis. Before the analyses, coated and uncoated foams were infiltrated with an epoxy resin, polished, and coated with a nanometric gold layer to be observed at the electron microscope.

Powder X-ray diffraction (XRD) spectroscopy was carried out using a Bruker D8 Advance. The analysis was performed at a scan speed of 2.4°•min^{-1}, in the 2θ range 5–80°, using Cu Kα radiation (λ = 0.15418 nm).

Thermogravimetric analysis (TGA) and differential scanning calorimetry (DSC) were performed by STA 449C Jupiter, Netzsch-Gerätebau GmbH, simultaneous analyzer. The analyses were conducted under the following conditions: temperature range of 20–1100 °C, heating ramp of 5 °C•min^{-1}, and airflow rate of 30 mL•min^{-1}.

The specific surface area (SSA) of the starting $Ni_{24}Mg_{56}Al_{20}$ powders has been calculated through the BET (Brunauer, Emmett, and Teller) method. The analysis has been carried out through a surface area analyser (SORPTY 1750 Fisons Instruments) on samples with a mass of about 0.1 g.

The redox properties of the samples were studied using a ThermoQuest Instrument TPD/R/O 1100 Catalytic Surface Analyzer. The analysis was carried out loading one layer of the foam sample following the subsequent steps: 1. Pretreatment under He flow (20 mL•min^{-1}): (i) temperature increment from 50 °C to 150 °C with a heating rate of 10 °C•min^{-1}; (ii) holding at 150 °C for 30 min; (iii) cooling until 50 °C is reached; 2. Reduction under 5 vol% H_2/He mixture (20 mL•min^{-1}): (i) temperature increment from 50 °C to 900 °C with a heating rate of 10 °C•min^{-1}; (ii) holding at 900 °C for 30 min; (iii) cooling until 50 °C is reached; 3. Oxidation under 5 vol% O_2/He mixture (20 mL•min^{-1}): (i) temperature increment from 50 °C to 900 °C with a heating rate of 10 °C•min^{-1}; (ii) holding at 900 °C for 30 min; (iii) cooling until 60 °C is reached. To close the cycle, another step of reduction was carried out. The gas mixtures were fed to the reactor, in which the sample was placed, and the outlet gas stream passed firstly into a trap to eliminate H_2O traces developed during reduction cycles and then was analyzed by a Thermal Conductivity Detector (TCD). Through data processing, it was possible to obtain reduction and oxidation profiles as a function of temperature, hence, the amounts of the various species that were reduced/oxidized were detected.

Raman analysis was carried out with a micro-spectrometer Raman RM1000 (Renishaw/Thermo Fisher, New Mills, Wotton-under-Edge, Gloucestershire, UK) interfaced to a microscope Leica DMLM (objective 5 × , 20 × . 50 ×). The available sources were an Ar^+ laser (λ = 514.5 nm; P_{out} = 25 mW) and a diode laser (λ = 780.0 nm; P_{out} = 30 mW). In order to eliminate the Rayleigh scattering, the system was equipped with a notch filter for the Ar^+ laser and an edge filter for the diode one. The network was a monochromator with a pass of 1200 lines•mm^{-1}. The detector was a CCD one (Charge-Coupled Device) with a thermo-electrical cooling (203 K).

Further characterizations on NiMgAl LDH derived catalyst can be found in Ref. [38].

2.4. Catalytic test

The structured catalysts ($Ni_{24}Mg_{56}Al_{20}$ @ NiCrAl foam, labelled NiMgAl foam) were prepared by punching the impregnated NiCrAl in discs of 1 cm in diameter, that were then stacked (7 layers) and thermo-pressed (MemoPresse, Mod. 50 P, 150 °C, ≈450 bar, 60 s) in order to obtain a structured catalysts of 1 cm height. The as-obtained catalysts were finally thermally treated at 900 °C for 1h. Conventional pellets of $Ni_{24}Mg_{56}Al_{20}$ (labelled NiMgAl pellets) were obtained by pressing the powder in tablets, then crushed and sieved between 30 and 40 mesh, to be considered for comparison purposes.

The catalysts were evaluated in a fixed-bed reactor comprising a tubular INCOLOY 800HT reactor (length: 500 mm; internal diameter: 10 mm) placed inside a programmable furnace. A sliding thermocouple was used to monitor the temperature of the catalytic bed. A total of 0.7854 cm^3 of catalyst (14–20 mesh) was loaded into the reactor. Reduction to metallic nickel was performed by flowing a gas mixture of H_2/N_2 (10:90 v/v) at 500 mL•min^{-1}, initially at 500 °C for 1 h to avoid the presence of hotspots on catalyst surface due to exothermicity of the reduction process, also considering the high amount of Ni content especially in the pelletized catalyst, followed by 750 °C for 3 h. Deionized water was delivered via a JASCO HPLC pump and fully vaporized before mixing with preheated oxygen. The wet effluent gas passed through a condenser maintained at approximately 0 °C to remove water vapor before analysis by gas chromatography (GC). The dry gas was analyzed using an Agilent 490 micro-GC equipped with two columns: a 20 m MS5A column (carrier gas: N_2) for hydrogen separation and a 1 m COx column (carrier gas: He) for analyzing CH_4, CO, and CO_2. Both modules utilized thermal conductivity detectors (TCDs). The catalytic tests were conducted at ambient pressure with a gas hourly space velocity (GHSV) of 40000 h^{-1}. Feed composition and operating temperatures were determined based on thermodynamic studies performed using Aspen + software, simulating a biogas composition with a CH_4/CO_2 ratio of 60/40 and the point of thermo-neutrality. To assess the flexibility of the catalysts under variable conditions reflecting changes in renewable resource availability, tests were conducted across a range of parameters. These included temperature variations (tests 2–4), steam content (tests 6–8), and oxygen levels (tests 10–13). To evaluate catalyst stability, tests were performed at optimal thermodynamic conditions at the beginning and end of each parameter study (tests 1, 5, 9, and 14). The conditions used for the catalytic tests are summarized in the supporting Table S1. Methane and carbon dioxide percentage conversions were calculated based on the vol% of products and unreacted reagents measured via GC analysis, as reported in equations Eq. (5) and Eq. (6) for methane and carbon dioxide respectively, where X_G represents the reagent G percentage conversion, while $\dot{V}_{Gin}$ and $\dot{V}_{Gout}$ represent G volume flow rate inside and outside the reactor respectively (G = CH_4 or CO_2).

$$XCH_4 = 100 \cdot \frac{\dot{V}CH_{4in} - \dot{V}CH_{4out}}{\dot{V}CH_{4in}} \quad \text{(Eq. 5)}$$

$$XCO_2 = 100 \cdot \frac{\dot{V}CO_{2in} - \dot{V}CO_{2out}}{\dot{V}CO_{2in}} \quad \text{(Eq. 6)}$$

Experimental and equilibrium conversions were also reported in Table S1.

The syngas productivity expresses the outlet flow of syngas (flow of H_2 + flow of CO) over the mas of catalyst and it has been calculated as follows (Eq. (7)):

$$Syngas\ productivity\ \left(\frac{mL}{min \cdot g}\right) = \frac{H_{2\ OUT}\left(\frac{mL}{min}\right) + CO_{OUT}\left(\frac{mL}{min}\right)}{mass\ catalyst\ (g)} \quad \text{(Eq. 7)}$$

3. Results and discussion

3.1. Optimization of the suspension

$Ni_{24}Mg_{56}Al_{20}$ mixed oxides powder (SSA_{BET} = 120 $m^2\ g^{-1}$ and apparent density 0.996 g•cm^{-3}) was dispersed in water at a concentration of 2.5 wt% using a sonication probe and magnetic stirring simultaneously. Water was selected as a non-harmful, non-hazardous, and economical medium to properly disperse the oxides and the required additives. The as-obtained suspension was used for the physicochemical and colloidal characterization. A properly diluted (1:100 in mass) aliquot was prepared for the assessment of the zeta potential measured at the diluted suspension's natural pH (10.1) resulting in −6 ± 2 mV, Table 1. This absolute value was not high enough to grant a proper electrostatic stabilization of the suspension, in fact, it was observed a fast sedimentation. Three different commercial deflocculating agents were tested to increase the stability: Darvan 821-A, Dolapix CA, and Dolapix PC 21. Deflocculants were selected as negatively charged electro-steric agents, contributing to improve suspension stability thanks to both electrostatic and steric actions [15,43,44]. Titrations reported in Fig. 1, demonstrate how more negative zeta potentials can be achieved by increasing deflocculant concentration, until the plateau corresponding to the saturation of the particles' surface; for concentrations higher than 120 mg of deflocculant per g of powder, the zeta potential results close to −45 mV. The best behavior was observed for Dolapix PC 21, which grants a slightly more negative plateau zeta potential, close to −50 mV (Fig. 1). Therefore, this deflocculant was chosen for the stabilization of the suspensions.

Despite the use of an appropriate deflocculant, sedimentation phenomena were observed in the as-prepared aqueous suspension. As shown by the FE-SEM image reported in Fig. S1 the as-synthesized $Ni_{24}Mg_{56}Al_{20}$ starting powder shows a bimodal particle size distribution constituted by fine aggregates with a diameter below 1 μm and larger clusters with dimensions up to 100 μm.

A more accurate particle size analysis has been conducted at the suspension level, Table 1. The average hydrodynamic diameter of the colloidal fraction has been determined by DLS, resulting to be 350 ± 20 nm with a polydispersity index (PDI) value of 0.57 ± 0.06, representing a highly dispersed population, Fig. 2-a. The particle size distribution of the larger fraction constituted by micrometric aggregates has been evaluated by sedimentation analysis (Fig. 2-b), resulting in an estimated particle size of 16 ± 14 μm. The suspension's results are well aligned with the FE-SEM observations of the powder, indicating the presence of large aggregates and high polydispersity.

To reduce the presence of undesired aggregates and achieve a more homogenous and smaller-sized particle population, a high-energy ball-milling of the $Ni_{24}Mg_{56}Al_{20}$ raw powder has been performed [45]. DLS and sedimentation analyses were repeated on the milled suspension and comparisons between pre-milling (raw powder) and post-milling powders are reported in Fig. 2. For the post-milling powders the average hydrodynamic diameter is reduced to 239 ± 2 nm and a more homogenous distribution is obtained (Fig. 2-a), compared to the multimodal population of the raw material. This also results in a slightly lower PDI of 0.39 ± 0.01, which does not represent a perfectly monodisperse population, partially due to the presence of a micro-sized tail shown in the graph in Fig. 2-a. A longer milling treatment could lead to a smaller-sized and more homogenous population, but it was avoided in order to prevent possible damage to the active phase structure due to the high-energy process. The diameter reduction and distribution narrowing trends were even more pronounced in the analysis of the microscopic fraction, where the particles' average size was reduced from 16 ± 14 μm to 2 ± 6 μm (Fig. 2-b). The high-energy milling treatment significantly disrupted larger aggregates, resulting in a more suitable particle distribution for the deposition of the catalytic coating. As previously discussed, the milling was not further pursued to prevent structural damage to the active phase, since, as reported below, the suspension remained

Table 1
Comparison of the physicochemical properties of the $Ni_{24}Mg_{56}Al_{20}$ suspensions with pre- and post-milling powders. Particle size analysis including hydrodynamic diameter (φ_{DLS}), polydispersity index (PDI), and sedimentation diameter ($\varphi_{sedimentation}$). Suspension's stability investigation includes natural pH and zeta potential, isoelectric point (IEP), and deflocculant isoelectric point (deflocculant IEP).

Sample	φ_{DLS} (nm)	PDI	$\varphi_{sedimentation}$ (μm)	pH	Zeta potential (mV)	IEP (mV)	Deflocculant IEP ($mg \bullet g^{-1}$)
Pre-milling	350 ± 20	0.57 ± 0.06	16 ± 14	10.1	−6 ± 2	9.1	0.7
Post-milling	239 ± 2	0.39 ± 0.01	2 ± 6	9.8	44.2 ± 0.5	>12.9	59.7

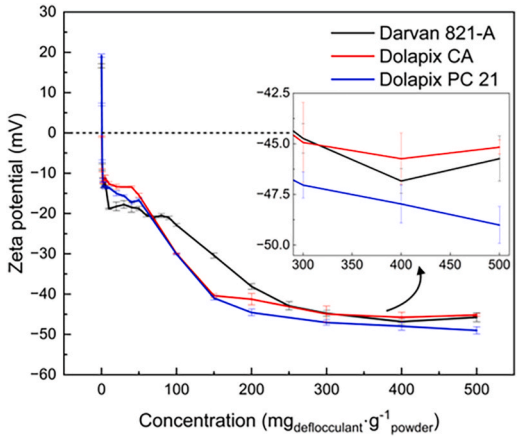

Fig. 1. Titrations of the zeta potential as a function of the deflocculant's concentration, reported as milligrams of deflocculant per gram of powder: Darvan 821-A (black), Dolapix CA (red), and Dolapix PC 21 (blue). A magnification of the curves in the 300–500 $mg \bullet g^{-1}$ concentration range is reported in the inset. (For interpretation of the references to colour in this figure legend, the reader is referred to the Web version of this article.)

stable for the subsequent operations.

To better understand the behavior of the material once dispersed in water, a titration of the zeta potential as a function of the pH was performed. As reported in Fig. 3-a, it is evident that the milling treatment strongly affects the properties of the powders and consequently their zeta potential. The post-milling suspension exhibited a highly positive zeta potential of 44.2 ± 0.5 mV at its natural pH (9.8), indicating a strong electrostatic contribution to the colloidal stability (Table 1). This effect, combined with a smaller particle size distribution, resulted in a stable suspension suitable for dip-coating.

For what concerns the pH titrations, the isoelectric point (IEP) was shifted to a more basic pH, increasing from 9.1 for the pre-milling powder to a value higher than 12.9 for the post-milling powder (Table 1). Along with the IEP, the whole curve reported in Fig. 3-a was shifted, indicating that a higher OH^- concentration was required to reach a negative zeta potential. This may be due to the reduction of the particle size, exposing a larger surface area of the layered double hydroxide structure of the material, requiring a higher concentration of OH^- ions to reach a negative zeta potential.

Even if the post-milling suspension demonstrated excellent stability without adding a deflocculant, the titration of the zeta potential as a function of the concentration of Dolapix PC 21 was conducted, and results are reported in Fig. 3-b. The comparison between the pre- and post-milling samples revealed that, like the pH titration, a higher amount of deflocculating agent was required to reach a negative zeta potential (0.7 $mg \bullet g^{-1}$ pre-milling vs. 59.7 $mg \bullet g^{-1}$ post-milling, concentration reported as milligrams of deflocculant per gram of powder). Additionally, the post-milling sample exhibited a more negative plateau, shifting from −50 mV pre-milling to −60 mV post-milling. This phenomenon confirmed that the reduction of the particle's size due to the milling increased the sample's exposed surface area, allowing it to accommodate a larger amount of Dolapix PC 21. The titrations of the zeta potential as a function of pH or deflocculant concentration confirmed the previous observations: the milled suspension did not require further stabilizers. Therefore, this system, without the need for deflocculants or pH adjustments, will be used for the study of the binder.

The binder plays a key role in the processing of ceramic suspensions, as it can strongly influence the viscosity of the material. The binder can also improve the stability of the suspension, mainly thanks to its steric hindrance. To achieve a successful and homogenous deposition via dip-coating, it is fundamental to modulate the viscosity of the sample, as both withdrawal speed and viscosity are crucial parameters for this technique [46]. Typically, a faster withdrawal speed and higher viscosity are correlated with thicker coatings [47].

Dip-coating performs properly in a specific viscosity (1–500 mPa•s) and shear rate (1-100 s^{-1}) range, working with a Newtonian fluid, with optimal values depending on the substrate and the suspension [21–23, 48,49]. For this study, we selected two types of binders: hydroxypropyl cellulose (HPC) and polyvinyl alcohol (PVA). The comparison between HPC and PVA has been performed working with a 2.5 wt% suspension of $Ni_{24}Mg_{56}Al_{20}$ milled powder, loaded with the same amount, 2.5 wt%, of either HPC or PVA. Results reported in Fig. S2 highlighted a predominantly Newtonian behavior (constant viscosity as a function of the shear rate) for both binders. However, HPC provided a higher viscosity, ≈27

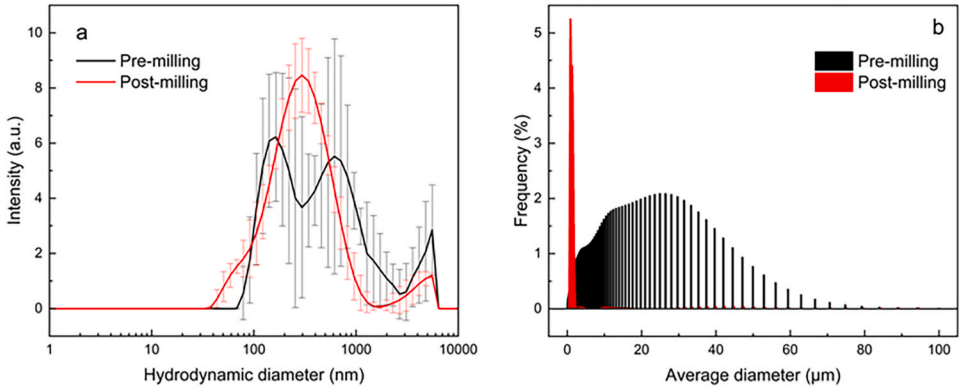

Fig. 2. Particle size analyses of pre- and post-milled $Ni_{24}Mg_{56}Al_{20}$ powder: (a) hydrodynamic diameter distribution assessed by DLS and (b) particle size distribution measured by sedimentation analysis.

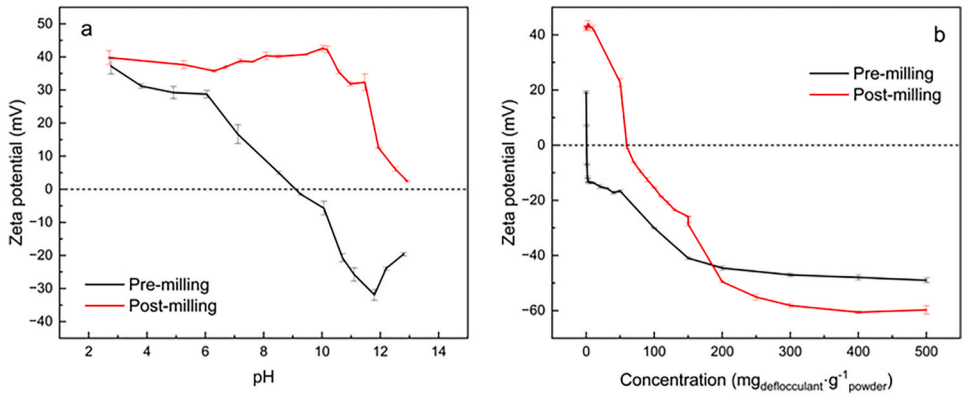

Fig. 3. Zeta potential titrations of pre- and post-milling sample: (a) as a function of the pH and (b) as a function of the deflocculant's concentration reported as milligrams of deflocculant per gram of powder.

mPa•s, compared to PVA ≈2.4 mPa•s and the suspension without additives ≈1.8 mPa•s, making it more suitable for the desired application. After this first screening, HPC was selected as the binder for the dip-coating formulation. Further rheological investigations for the suspensions using HPC as a binder and Dolapix PC 21 as a deflocculant were performed. As shown in Fig. S3, the suspension containing milled powder, HPC, and Dolapix PC 21 was characterized by higher viscosity and non-Newtonian behavior, not suitable for dip-coating. Since the suspension was stable without Dolapix PC 21, these rheological complications led to the decision to avoid the use of deflocculants.

Contact angle measurements demonstrated slightly hydrophobic properties of the NiCrAl foam against the water-based suspension. In fact, once a sessile drop of the $Ni_{24}Mg_{56}Al_{20}$ suspension was deposited on the substrate, contact angles greater than 90° were recorded (Table 2). Pre-milling suspension was correlated to higher contact angles compared to the equivalent post-milling compositions. Furthermore, the suspension with hydroxypropyl cellulose exhibited less hydrophobic behavior and a time-dependent change in the contact angle, with decreasing values observed after 30 and 60 s, as shown in Fig. S4.

To achieve a perfect wettability of the catalyst's support and to reduce bubble generation during suspension processing, Surfynol SE-F surfactant was implemented in the formulation. The surfactant action lowered the surface tension of the suspension, and a 0.15 wt% concentration of Surfynol SE-F led to the instantaneous permeation of the foam. In this way, a more homogeneous coating should be produced. Viscosity measurements confirmed that adding Surfynol SE-F did not change the rheology of the sample. In fact, the viscosity profiles of the suspension with and without Surfynol SE-F were perfectly superimposable (Fig. S5).

3.2. Dip-coating

The optimized suspension ($Ni_{24}Mg_{56}Al_{20}$ 2.5 wt%, HPC 2.5 wt%, Surfynol SE-F 0.15 wt%) was used for the production of the catalyst via dip-coating. As described in the Experimental section, NiCrAl oxidized foams were dipped with controlled immersion and withdrawal speeds, oven-dried, and the deposition repeated up to four times. The final product was thermally treated in a furnace. Previous dilatometric analysis demonstrated the thermal stability of the oxidized NiCrAl foam up to approximately 1000 °C. The maximum thermal expansion coefficient ($16•10^{-6}$ °C^{-1}) was recorded at 1100 °C, corresponding to the foam softening and coefficient reduction [42]. The thermal behavior, up to 1100 °C, of the coating suspension and the foam substrate was studied by TGA-DSC, and results revealed good stability of the substrate and the consolidation of the active phase at the processing temperature of 900 °C, supporting Fig. S6–a and Fig. S6–b.

The selected dip-coating conditions (immersion and withdrawal speed 0.1 mm•s^{-1}, residence time 300 s, drying 120 °C for 30 min) allowed the deposition of a thin layer of the $Ni_{24}Mg_{56}Al_{20}$ active phase on the NiCrAl substrate. To improve the homogeneity of the coating and the active phase load, up to four deposition cycles were performed. In Fig. 4, the amount of material deposited during the process is reported. It is interesting to note the comparison between $Ni_{24}Mg_{56}Al_{20}$ dispersed in water (black) and the optimized suspension (red): the combination of hydroxypropyl cellulose and Surfynol used as binder and surfactant respectively, enhanced the material deposition about six times, leading

Table 2
Contact angle analysis. Measurements were repeated after 0, 30, and 60 s after the drop deposition over the NiCrAl substrate. Comparison of the results achieved using pre- and post-milling powder, with or without the use of HPC as a binder.

Treatment	Sample	Contact angle (°) t = 0 s	Contact angle (°) t = 30 s	Contact angle (°) t = 60 s
Pre-milling	NiMgAl	130 ± 3	129 ± 3	129 ± 3
Pre-milling	NiMgAl + HPC	128 ± 2	116 ± 8	115 ± 8
Post-milling	NiMgAl	125 ± 1	124 ± 1	124 ± 1
Post-milling	NiMgAl + HPC	113 ± 10	99 ± 10	97 ± 11

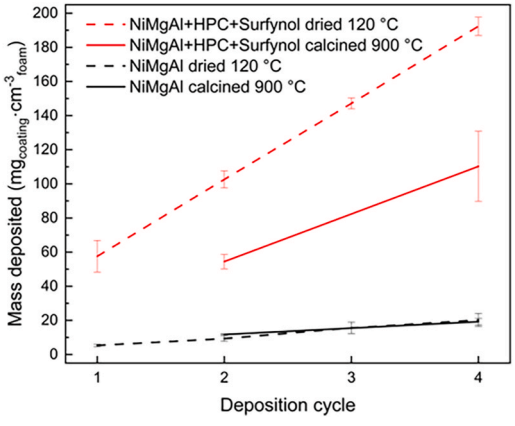

Fig. 4. Mass deposited after consecutive dip-coating cycles, reported as milligrams of coating per cubic centimetre of NiCrAl foam. Comparison between the NiMgAl powder suspension (black) and the NiMgAl + HPC + Surfynol optimized suspension (red). Solid lines represent the inorganic load measured after calcination (900 °C, 1 h), and dashed lines represent the total load measured after the drying step (120 °C, 30 min). (For interpretation of the references to colour in this figure legend, the reader is referred to the Web version of this article.)

to an active phase load of 110 ± 21 mg•cm^{-3} (milligrams of coating per cubic centimetre of foam) after 4 depositions. The dashed lines reported in Fig. 4 represent the mass of coating deposited and measured after the drying step at 120 °C, including both the inorganic and organic compounds, while the solid lines represent the mass of coating weighted after the calcination at 900 °C, related only to the final inorganic coating constituted by the $Ni_{24}Mg_{56}Al_{20}$ mixed oxides active phase. For the water dispersion, the solid and dashed lines are perfectly superimposable since no organic additives were present. Conversely, for the optimized suspension, formulated with a 1:1 wt ratio between the HPC and powder, a strong correlation was observed, with twice the mass detected before the additives burn out during the calcination.

3.3. Fresh catalyst characterization

The as-obtained metallic foams coated with the Ni-based catalyst were characterized through SEM analyses. The SEM micrographs reported in Fig. 5 compare the bare NiCrAl foam (surface Fig. 5-a, cross-section Fig. 5-b) to the sample coated by $Ni_{24}Mg_{56}Al_{20}$ (specimen photo Fig. 5-c, cross-section at different magnifications Fig. 5-d,e,f). It is possible to observe a micrometric coating homogenously distributed over the substrate, with a slightly higher accumulation on the external surfaces.

The elemental composition of the catalyst was confirmed by EDX analysis reported in Fig. S7 and Fig. S8 of the supporting information. Results showed the elements constituting the substrate (Ni, Cr, Al) and the active phase coating (Ni, Mg, Al). The element maps reported in Fig. S7 made clearly visible the different compositions of the substrate compared to the coating.

The crystalline structure of the $Ni_{24}Mg_{56}Al_{20}$ powder during the different steps of the catalyst production was studied by XRD (Fig. 6). The starting material (Fig. 6-Raw calcined) was constituted mainly by nickel-magnesium mixed oxide phase (PDF 24–0712, cF8), while the magnesium-aluminium spinel (PDF 74–1132, cF56) was nearly undetected, also because of partials superimposition of peaks. The crystal size calculated using the Scherrer equation was 4.7 ± 0.3 nm.

Due to the LDH memory effect, once the mixed oxide powder is dispersed into water, it hydrates and regains the typical LDH structure with mixed hydroxides [50–52]. In fact, after the wet milling, the dried powder (Fig. 6-Milled dried) revealed the typical layered double hydroxide (PDF 48–0601) XRD pattern, coupled with the peaks related to the nickel-magnesium mixed oxide, indicating that the hydration process was not quantitative. After the wet milling treatment, the calculated crystal size of the LDH phase was 8 ± 1 nm.

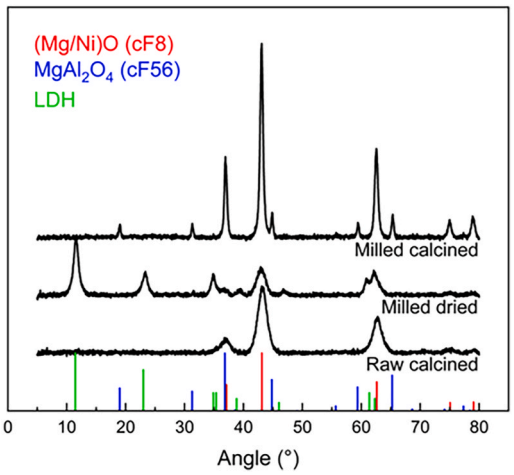

Fig. 6. XRD diffractograms of 1) starting mixed oxide phase (Raw calcined) powder, 2) the powder after wet planetary milling (Milled dried); 3) Planetary milled powder after calcination at 900 °C × 1h (Milled calcined).

It is important to verify the final crystal structure of the calcined catalyst to check the formation of the desired mixed oxides phase. The study demonstrated that the calcination (900 °C for 1 h) performed on the wet-milled powder led to the formation of the desired mixed oxide phase with increased crystallinity compared to the starting raw material (Fig. 6-Milled calcined). After the thermal treatment, peaks are more intense and sharper, allowing the detection of well-resolved nickel-magnesium mixed oxide (PDF 24–0712, cF8) and magnesium-aluminium spinel (PDF 74–1132, cF56) peaks, with an average crystal size calculated of 19 ± 4 nm.

For the fabrication of the structured catalyst (NiCrAl-foam-supported $Ni_{24}Mg_{56}Al_{20}$, labelled as NiMgAl foam) for catalytic tests, the typical dip-coated substrate (6 x 5 × 1.6 cm^3) was punched in discs of 1 cm in diameter, after the oven drying step (120 °C for 30 min). The discs were then stacked and thermo-pressed to produce a multi-layered catalyst (7 layers: Ø = 1 cm, h = 1 cm). The hydroxypropyl cellulose still present in the coating helped stack and attach the layers, subsequently the organic was burned out during the calcination step (900 °C, 1 h) which also

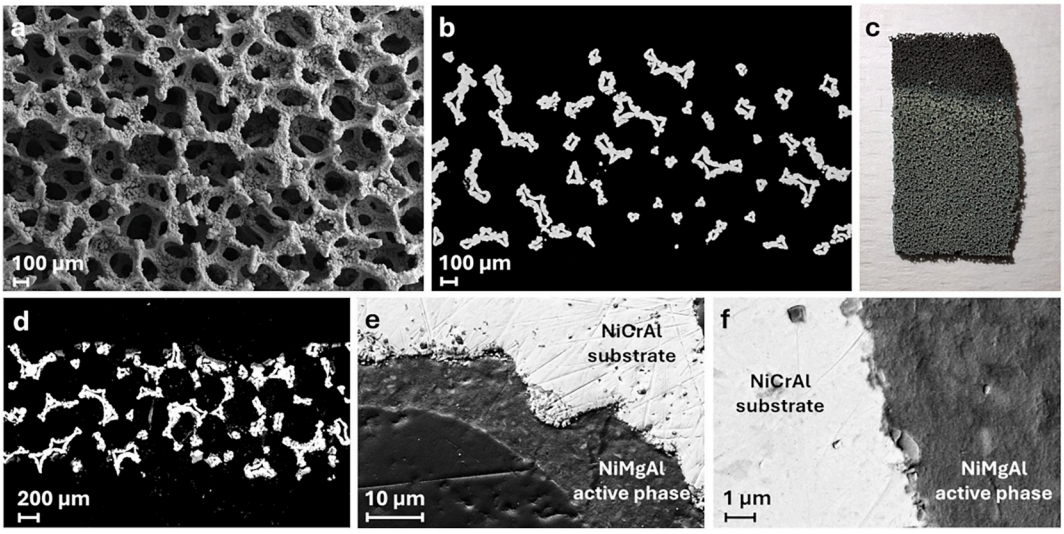

Fig. 5. FE-SEM images (a, b, d, e, and f) and photo (c) of the NiCrAl before and after the dip-coating: (a) surface of the uncoated foam; (b) cross-section of the uncoated foam; (c) photo of the specimen after the dip-coating, the upper and darker part of the substrate was not immersed in the $Ni_{24}Mg_{56}Al_{20}$ suspension; (d) cross-section of the coated substrate; (e) and (f) magnification of the catalyst coating layer.

developed the mixed oxide catalytic phase (previously demonstrated by XRD analysis, Fig. 6) and consolidate the 3D structure of the catalytic system (Fig. 7).

3.4. Catalytic performance testing

Two different types of catalysts were tested in the TRM conditions: conventional $Ni_{24}Mg_{56}Al_{20}$ (NiMgAl) pellets and the structured catalysts (NiMgAl foam) optimized in this work.

The first test was periodically repeated after completing each subsequent test set, to compare the reaction performances under the same conditions (see Table S1). These tests were conducted under uniform conditions: a temperature of 800 °C, a pressure of 1 atm, a gas feed ratio of $CH_4/CO_2 = 1.5$, $O_2/CH_4 = 0.5$, and $S/CH_4 = 0.2$, with a gas hourly space velocity (GHSV) of 40000 h^{-1}. These standardized conditions allowed for a direct comparison of the catalysts' stability and flexibility after being subjected to varying reaction environments, i.e., variation of temperature (tests 2–4), steam content (tests 6–8), and oxygen content (tests 10–13).

The results related to the catalytic activity of the two catalysts, i.e., pellets and structured ones, at the standard conditions are summarized in Fig. 8, and also compared with a non-coated foam. Both catalysts exhibited a stable methane conversion and a slight decline in carbon dioxide conversion after more than 17 h on stream. However, the structured catalyst demonstrated superior performance, achieving higher syngas productivity compared to the catalyst prepared through the pelletized NiMgAl catalyst, thanks to the lower amount of catalyst employed and to increased CO_2 conversion. Regarding this, the dry reforming reaction can be seen as the combination of reverse water gas shift and steam reforming. As the reverse water gas shift is an equilibrium and fast reaction under these conditions, the conversion of CO_2 can help us to have a hint on the exit temperature of the catalytic bed [5]. A higher CO_2 conversion is observed when the structured catalyst is used. On pelleted beds, the temperature in the catalytic bed follows a first increase due to exothermic reactions followed by a decrease due to endothermic ones, resulting in a low exit temperature hence lower conversion. The use of a foam as catalytic support allows to increase the heat exchange and homogenize the bed temperature increasing the exit one and thus the occurrence of reverse WGS and dry reforming leading to higher CO_2 conversion.

As a comparison and to exclude a significant contribution from the material that composes the foam, tests with bare foams were conducted. The limited activity observed with the non-coated foam can likely be attributed to the presence of nickel within the foam's structure. However, this activity diminishes noticeably over time, primarily due to the oxidation of the non-stabilized small quantity of nickel present in the material.

Minimal variations in the H_2:CO ratios, i.e., between 1.0 and 1.2, were observed for both catalysts, which is a significant advantage, particularly for maintaining a stable syngas composition for downstream applications.

In Fig. 9, the results of the catalytic tests are shown as a function of the reaction conditions, reported as the percentage conversion of CH_4 and CO_2, along with the syngas productivity expressed in millilitres of syngas produced per minute, normalized by the mass of the NiMgAl active phase. Fig. 9-a presents the catalytic performance results for the TRM, evaluated at different reaction temperatures. In accordance with TRM thermodynamic predictions, catalytic efficiency increases with temperature, reaching peak performance at 800 °C. Variations in catalytic behaviour among the different catalysts are evident, with NiMgAl foam showing superior performance. The influence of water content on the catalytic activity is presented in Fig. 9-b. The catalytic system achieves nearly complete methane conversion under all tested conditions. However, CO_2 conversion exhibits a slight decline as the water content increases, likely due to the promotion of the steam reforming (SR) pathway at the expense of dry reforming of methane (DRM) and reverse water gas shift. Finally, Fig. 9-c highlights the influence of the O_2/CH_4 on reaction performance. Although modest amounts of oxygen are essential for achieving the autothermal condition of the reaction, an increase in oxygen leads to a lower CO_2 conversion, while methane conversion remains nearly constant. The excess oxygen present in tests performed at standard conditions may contribute to the occurrence of catalytic partial oxidation, in place of steam reforming, dry reforming and reverse WGS and to the formation of more pronounced hot spots at the top of the catalytic bed. This, in turn, could hinder the performance of the catalyst due to sintering and oxidation phenomena on the nickel active phase.

A comprehensive analysis of the catalytic properties of the samples and their performance in the TRM process, following the procedure described in the Experimental part ("Catalytic test" section), reveals that the most significant results were obtained with the structured catalytic systems. In fact, although the performances in terms of syngas productivity, methane, and carbon dioxide conversion are just slightly higher for the structured catalysts, it must be noted that the amount of catalyst deposited on the foam is around an order of magnitude lower than that of the pellets. The actual calculation of syngas productivity relative to the catalyst mass in the catalytic bed is shown in Figs. 8 and 9, clearly highlighting the difference between the two catalytic systems in terms of efficient utilization of active area for the same catalytic bed volume. The improved process can be attributed to several key factors: (i) a better heat exchange in the case of the foam, which reduces hot and cold spots which may affect the activity and stability, thanks to the low amount of catalyst deposited and the high thermal conductivity of the foam [53], (ii) a more important open porosity, synonym of more efficient use of the active metal, (iii) reduced pressure drops, resulting in decreased resistance to gas flow through the reactor, (iv) improved mechanical stability and durability, and (v) fewer diffusion limitations thanks to the deposition of a thin catalytic layer over the foam structures. The decrease in carbon dioxide conversion observed in Test 14 for the NiMgAl foam sample can be attributed to partial re-oxidation of nickel (Ni) during the oxygen content flexibility tests, as confirmed by the temperature-programmed reduction (TPR) analysis (Fig. 10). Notably, an increase in hydrogen uptake was detected in the spent sample, indicating a higher concentration of nickel oxide (NiO) and,

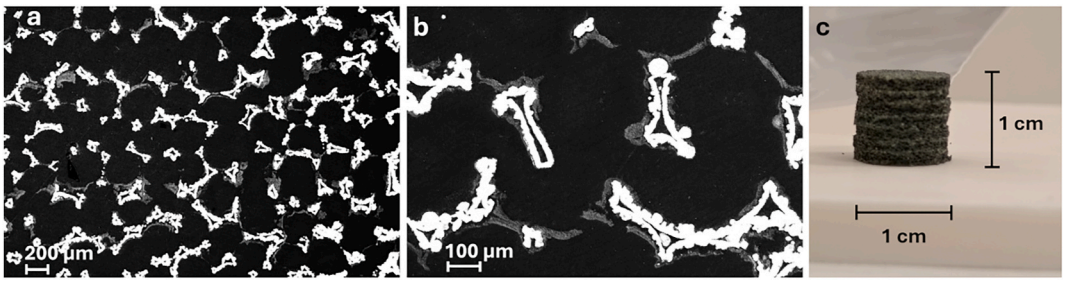

Fig. 7. Final structured NiMgAl foam catalyst. (a) and (b) FE-SEM images taken at different magnifications of the stacked layers obtained by pressing and calcinating the dip-coated foam. (c) photo of the catalytic cylinder with a diameter and height of 1 cm.

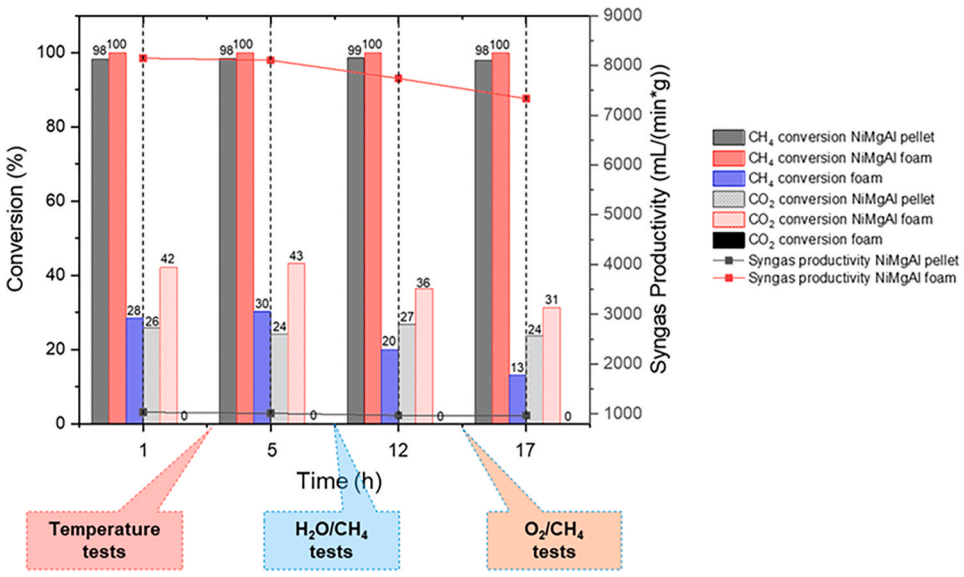

Fig. 8. Comparison of catalytic test results on NiMgAl pellet, NiMgAl foam, and non-coated foam. Reaction conditions: 800 °C, 1 atm, CH_4:CO_2 = 1.5; O_2:CH_4 = 0.5, S:CH_4 = 0.2 and GHSV 40000 h^{-1}.

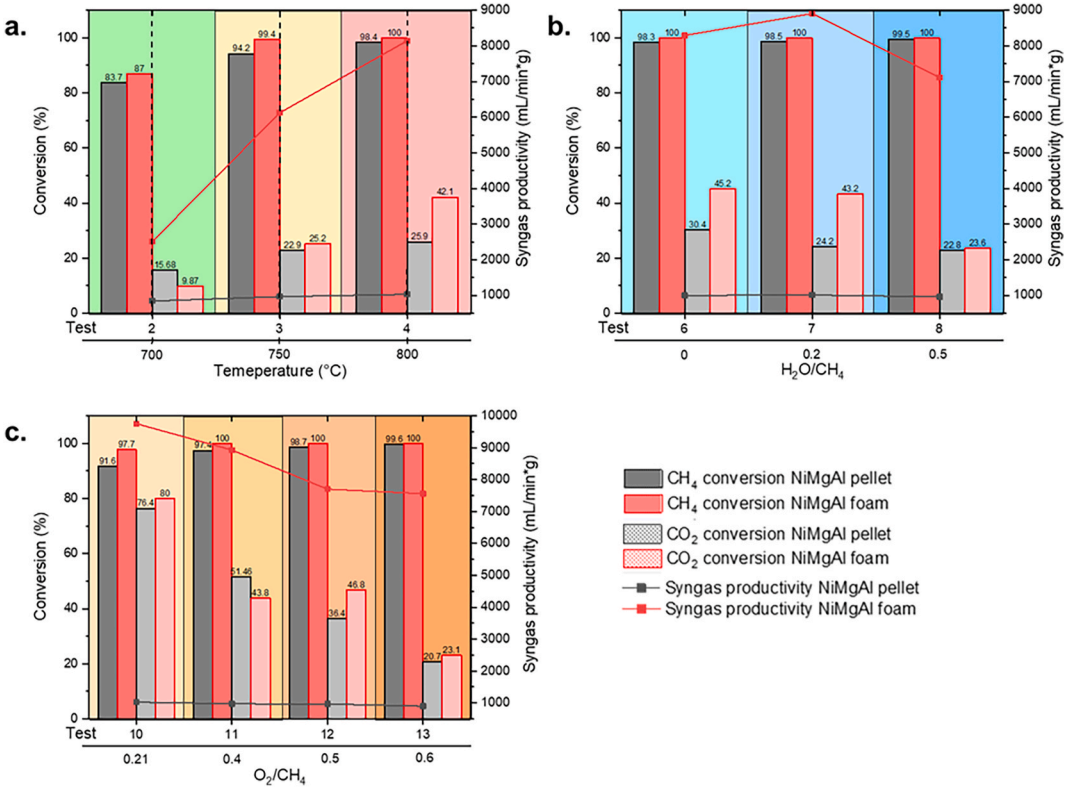

Fig. 9. Comparison of catalytic test results on NiMgAl pellet and NiMgAl foam. (a) Reaction conditions: [700–800] °C, 1 atm, CH_4:CO_2 = 1.5; O_2:CH_4 = 0.5, S:CH_4 = 0.2 and GHSV 40000 h^{-1}; (b) Reaction conditions: 800 °C, 1 atm, CH_4:CO_2 = 1.5; O_2:CH_4 = 0.5, S:CH_4 = [0–0.5] and GHSV 40000 h^{-1}; (c) Reaction conditions: 800 °C, 1 atm, CH_4:CO_2 = 1.5; O_2:CH_4 = [0.21–0.6], S:CH_4 = 0.2 and GHSV 40000 h^{-1}.

consequently, catalyst deactivation. This deactivation, which was due to the increase in the oxygen feed during the tests, can be avoided by working at a lower oxygen content, hence increasing the catalyst stability.

Finally, the investigation of varying reaction conditions identified the most promising approach for achieving high hydrogen productivity alongside enhanced reactant conversions. Previous findings [12,54,55] underscore the critical importance of attaining a CO_2 conversion rate exceeding 60 % for the TRM process to be considered competitive with conventional fossil-based reforming methods. Moreover, it is important to emphasize that the TRM of biogas does not directly release fossil-derived CO_2. Instead, the CO_2 generated during the process originates from the degradation of biomass, which had previously absorbed atmospheric CO_2 during its growth. Operating at a temperature of 800 °C, a pressure of 1 atm, and a gas feed ratio of CH_4/CO_2 = 1.5, O_2/CH_4 = 0.21, and S/CH_4 = 0.2, with a gas hourly space velocity

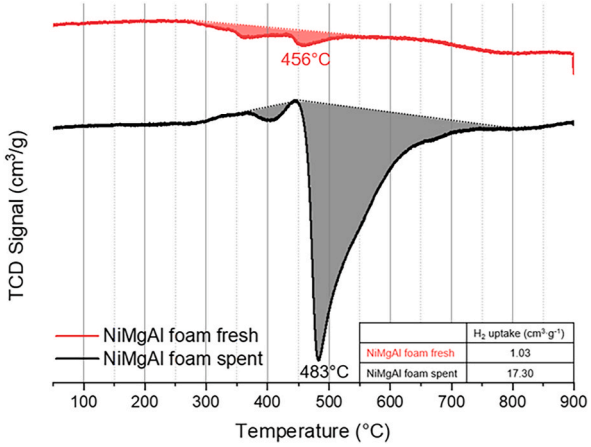

Fig. 10. TPR analysis of NiMgAl foam before (fresh) and after (spent) the catalytic test.

(GHSV) of 40000 h^{-1}, allows the process to achieve CO_2 conversion rates exceeding 75 % (Fig. 11). This substantially enhances the efficiency of the process, leading to an improvement in carbon dioxide conversion of over 200 % compared to the standard reaction conditions. This significant increase may be attributed to the milder reaction conditions adopted during this test. Specifically, the presence of excess oxygen in the previous tests could have led to the formation of more pronounced hot spots at the top of the catalytic bed, which may in turn reduce the performance of the reforming reactions (both of which are highly endothermic) and potentially deactivate the nickel active phase due to sintering and reoxidation phenomena.

3.5. Spent catalyst characterization

Raman analysis was conducted to probe the eventual presence of carbon formed during the reaction (Fig. 12). Deactivation by formation of carbon over the structured catalyst can be excluded by the results of Raman analysis, which showed the presence of carbon only on the pelleted catalyst though considering the difficulties in conducting this analysis on a 3D sample in the case of the dip-coated foam. The absence of coke in the case of the structured catalyst may be due to a more homogeneous heat distribution that avoided hot spots in the first part of the catalytic bed, where exothermic reactions occur and cold spots in the last part of the catalytic bed, where the endothermic reactions occur. This unfavoured coke forming reactions like methane decomposition

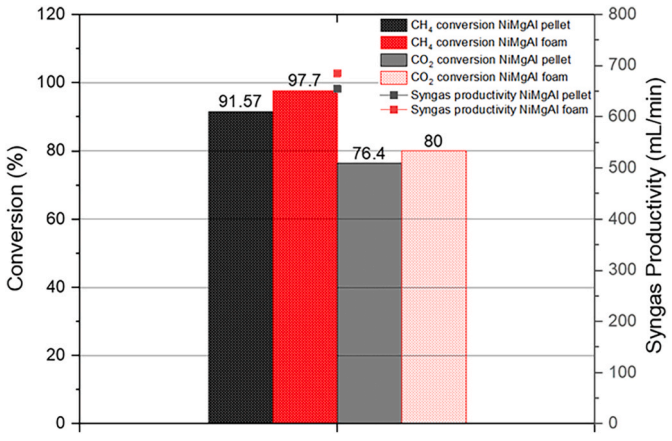

Fig. 11. Comparison of catalytic test results on NiMgAl pellet and NiMgAl foam. Reaction conditions: 800 °C, 1 atm, CH_4:CO_2 = 1.5; O_2:CH_4 = 0.21, S: CH_4 = 0.2 and GHSV 40000 h^{-1}.

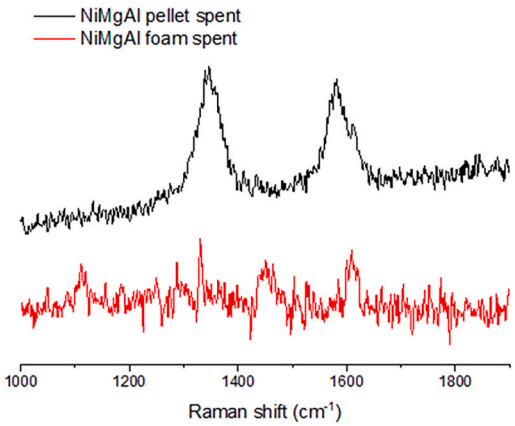

Fig. 12. Raman analysis: comparison of the carbon formation on the pelleted and structured spent catalysts.

and CO disproportionation in those hot and cold spots.

XRD analysis was also conducted on the top and bottom of the foam (which indeed is submitted respectively to oxidative and reductive conditions due to the consumption of oxygen and steam and the production of hydrogen along the catalytic bed), Fig. S9. Typically, the evolution upon calcination at 900 °C of the LDH systems involves the segregation of an oxide phase (MgO) and a spinel one ($MgAl_2O_4$) is observed, with Ni being distributed in the two phases (Fig. 6, Milled calcined). After reduction the extraction of Ni^0 nanoparticles occurs by exsolution [38,56–58] with some Ni which might remain in the oxides (mainly spinel), depending on LDH composition and reduction conditions.

The XRD of the used catalysts show the presence of the following phases: a NiAl alloy representative of the metallic foam, a MgO and a spinel phases mainly due to $MgAl_2O_4$ phase typical of the catalyst also reported in Fig. 6, that can contain Ni and might have the contribution of a side $NiCr_2O_4$ phase deriving from foam oxidation and a metallic nickel phase deriving from the catalyst exsolution. Comparison of the XRD show a decrease in the peak intensity of Ni in the top part of the foam, which is the one exposed to oxidative conditions (high amount of oxygen and steam and low hydrogen content) indicating that the slight deactivation is related to Ni oxidation, consistently with the TPR results. Moreover, in the upper part of the foam catalytic bed a slight reflects related to Cr oxide has been observed, suggesting Cr oxidation from the foam.

To further analyse the phases and element distribution and to determine the condition of the coating layer after the catalytic tests SEM-EDX analyses were conducted on the spent structured catalyst (Fig. 10, 11 and 13). Cross-section images (Fig. 13-d and Fig. 13-e) confirm the integrity and strong adhesion of the coating after conducting TRM under different reaction conditions.

EDX elemental analysis was performed to see eventual changes in the composition of the coating and the distrubtion of the Mg and Al containing phases. From the maps reported in Fig. S10 it was possible to observe a homogenous magnesium-containing layer (indicative of the NiMgAl catalyst layer) on the surface of the chromium-containing substrate. Nickel and aluminium were evenly distributed all over the sample, as they are components of both the foam and the catalysts, while chromium was mainly concentrated in the inner structure, and magnesium was confined in the surface layer. Oxygen was detected as part of the mixed oxides structure, and carbon represented the intruded resin counterpart of the sample. These observations confirmed that dip-coating was a suitable process for depositing a homogeneous and durable coating consisting of a ceramic catalytic layer.

However, some areas containing a higher amount of Cr were observed. In particular, EDX analysis (Fig. S11) shows: (i) areas rich in Mg which can be related to MgO (also reported in the XRD of the milled

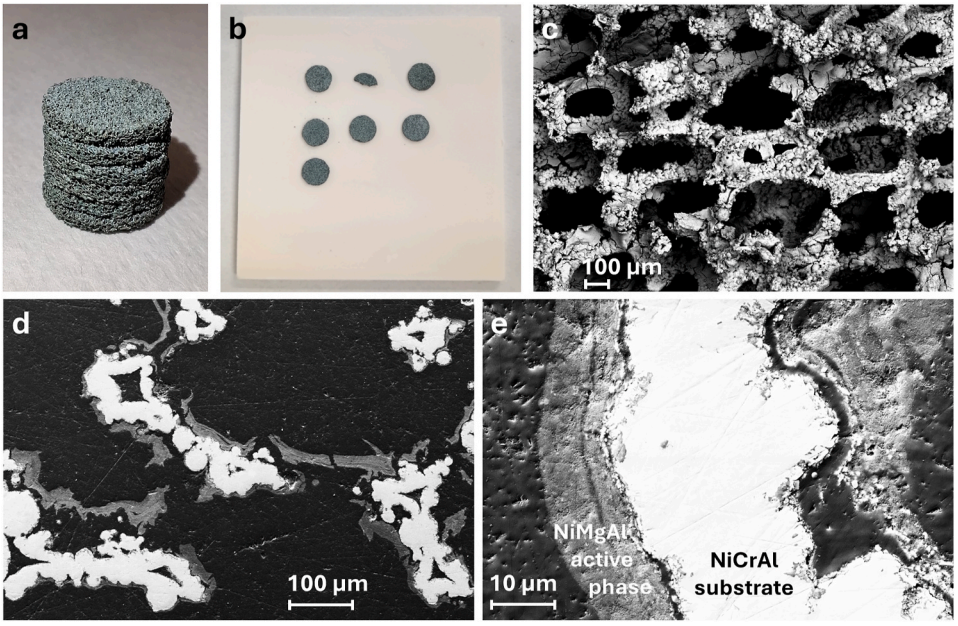

Fig. 13. Spent structured catalyst: (a) stacked catalyst; (b) delaminated layers; (c) FE-SEM image of the fracture surface of the external layer; (d) FE-SEM micrographs of polished cross-section image at low (d) and high (e) magnification.

calcined powder), (ii) areas with a Mg/Al ratio lower than the nominal one which is indicative of the presence of $MgAl_2O_4$ spinel and in general areas with different Mg/Al ratio which entails a different distribution of the MgO and $MgAl_2O_4$ phases in the sample, (iii) areas rich in Cr, related to the migration of this element from the foam and the formation of Cr oxide under oxidative conditions. The formation of Cr oxides and could influence foams stability under oxidative conditions at longer reaction times under oxidative conditions.

4. Conclusions

The dip-coating technique enabled the successful production of structured nickel-based catalysts for the tri-reforming of biogas. A synthesized nickel-based active phase (NiMgAl) was selected for its optimal balance between catalytic activity and cost-effectiveness. Nickel is effective in the studied reactions while being more affordable and widely available compared to noble metals. A commercial nickel-containing metal foam (NiCrAl) was used as a support due to its superior dispersion of the active phase compared to the pellet, enhanced thermal conduction, and the consequent reduction of hot spots that could accelerate the catalyst deactivation. Additionally, it offered lower pressure drop and minimized diffusion limitations. Optimizing the properties of the nickel, magnesium, and aluminium mixed oxides suspension was essential to ensure it met the requirements for effective dip-coating. Therefore, hydroxypropyl cellulose was used as a binder capable of achieving the rheological requirements, i.e. a fluid with Newtonian characteristics and a viscosity of approximately 27 mPa•s. Moreover, Surfynol SE-F was used as a surfactant to reduce surface tension and promote the wettability of the substrate, as confirmed by contact angle measurements. This, coupled with an accurate selection of the deposition parameters, allowed the deposit of a homogeneous layer of the active phase, as demonstrated by SEM-EDX analyses. The structured catalyst, with a diameter and height of 10 mm, was obtained by stacking and pressing 7 layers of coated foam. It demonstrated excellent performance in the TRM, outperforming the NiMgAl pellet overall, particularly the syngas productivity, expressed in millilitres of syngas produced per minute, normalized by the mass of the NiMgAl active phase employed, was about one order of magnitude higher. Using the NiMgAl foam, it was possible to achieve a conversion of 97.7 % and 80 % for CH_4 and CO_2, respectively, and syngas productivity higher than 9500 $mL•min^{-1}•g^{-1}$. The structured catalyst proved to be stable: no detachment of the coating was observed even after repeated cycles of use. From the TPR analysis, it was possible to confirm that the slight drop in CO_2 conversion observed after 17 h of use could be due to the partial re-oxidation of the nickel occurring during the oxygen content flexibility tests. These results highlight the promising potential of these materials for biogas tri-reforming. Future studies will focus on further optimizing the catalytic system to improve its stability, durability, and performance. In conclusion, this work demonstrates how a simple and economical technique, such as dip-coating, can be successfully employed to produce catalysts for the valorization of biomass, aligning with the principles of the circular economy.

CRediT authorship contribution statement

Andrea Brigliadori: Writing – original draft, Methodology, Investigation, Data curation. **Filippo Suzzi:** Methodology, Investigation, Formal analysis, Data curation. **Andrea Bartoletti:** Methodology, Investigation, Data curation. **Elisa Mercadelli:** Writing – review & editing, Supervision, Methodology. **Davide Gardini:** Methodology, Formal analysis, Data curation. **Elisabetta Orfei:** Writing – original draft, Methodology, Investigation, Data curation. **Andrea Fasolini:** Writing – original draft, Methodology, Investigation, Data curation, Conceptualization. **Jacopo De Maron:** Methodology, Investigation, Data curation. **Francesco Basile:** Writing – review & editing, Supervision, Project administration, Funding acquisition, Conceptualization. **Angela Gondolini:** Writing – review & editing, Supervision, Project administration, Funding acquisition, Conceptualization. **Alessandra Sanson:** Resources, Project administration, Funding acquisition.

Declaration of competing interest

The authors declare that they have no known competing financial interests or personal relationships that could have appeared to influence the work reported in this paper.

Acknowledgments

Authors acknowledge European funding from the Emilia-Romagna Region, H_2-Synergy - PR FESR 2021–2027 ACTION 1.1.2 CALL FOR STRATEGIC INDUSTRIAL RESEARCH PROJECTS TARGETING THE PRIORITIES OF THE SMART SPECIALIZATION STRATEGY REFERRED TO DGR 2097/2022 – S3 Area: Clean, safe and affordable energy (project number PG/2023/311159). The authors acknowledge financial support from PNRR MUR – M4C2 project PE00000021 "NEST - NETWORK 4 ENERGY SUSTAINABLE TRANSITION". The graphical abstract was created in BioRender. Bartoletti, A. (2025) https://BioRender.com/7e5qeq9.

Appendix A. Supplementary data

Supplementary data to this article can be found online at https://doi.org/10.1016/j.ijhydene.2025.150939.

References

[1] Neto AS, Wainaina S, Chandolias K, Piatek P, Taherzadeh MJ. Exploring the potential of syngas fermentation for recovery of high-value resources: a comprehensive review. Curr Pollut Rep 2025;11. https://doi.org/10.1007/s40726-024-00337-3.

[2] Sunkara S, Pankhedkar N, Gudi R. Valorization of refinery flue gas through tri-reforming and direct hydrogenation routes. Can J Chem Eng 2024;102:2136–50. https://doi.org/10.1002/cjce.25187.

[3] Zhang Y, Cui Y, Chen P, Liu S, Zhou N, Ding K, et al. Gasification technologies and their energy potentials. Elsevier B.V.; 2019. https://doi.org/10.1016/B978-0-444-64200-4.00014-1.

[4] Halmann M, Steinfeld A. Fuel saving, carbon dioxide emission avoidance, and syngas production by tri-reforming of flue gases from coal- and gas-fired power stations, and by the carbothermic reduction of iron oxide. Energy 2006;31:3171–85. https://doi.org/10.1016/j.energy.2006.03.009.

[5] Ertl G, Knözinger H, Weitkamp J. Handbook of heterogeneous catalysis, vols. 1–5; 2008. https://doi.org/10.1524/zpch.1999.208.part_1_2.274.

[6] Fasolini A, Mafessanti R, Abate S, Gramazio P, De Maron J, Centi G, et al. Integration of catalytic methane oxy-reforming and water gas shift membrane reactor for intensified pure hydrogen production and methanation suppression over Ce0.5Zr0.5O2 based catalysts. Catal Today 2023;418:114047. https://doi.org/10.1016/j.cattod.2023.114047.

[7] Pham XH, Ashik UPM, Hayashi JI, Pérez Alonso A, Pla D, Gómez M, et al. Review on the catalytic tri-reforming of methane - part II: catalyst development. Appl Catal Gen 2021;623. https://doi.org/10.1016/j.apcata.2021.118286.

[8] De Maron J, Mafessanti R, Gramazio P, Orfei E, Fasolini A, Basile F. H2 production by methane oxy-reforming: effect of catalyst pretreatment on the properties and activity of Rh-Ce0.5Zr0.5O2 synthetized by microemulsion. Nanomaterials 2023;13. https://doi.org/10.3390/nano13010053.

[9] Schiaroli N, Battisti M, Benito P, Fornasari G, Di Gisi AG, Lucarelli C, et al. Catalytic upgrading of clean biogas to synthesis gas. Catalysts 2022;12. https://doi.org/10.3390/catal12020109.

[10] Soleimani S, Lehner M. Tri-reforming of methane: thermodynamics, operating conditions, reactor technology and efficiency evaluation—A review. Energies 2022;15. https://doi.org/10.3390/en15197159.

[11] Schiaroli N, Lucarelli C, Iapalucci MC, Fornasari G, Crimaldi A, Vaccari A. Combined reforming of clean biogas over nanosized Ni–rh bimetallic clusters. Catalysts 2020;10:1–17. https://doi.org/10.3390/catal10111345.

[12] Alli RD, de Souza PAL, Mohamedali M, Virla LD, Mahinpey N. Tri-reforming of methane for syngas production using Ni catalysts: current status and future outlook. Catal Today 2023;407:107–24. https://doi.org/10.1016/j.cattod.2022.02.006.

[13] Thyssen VV, Avp Lino, Assaf JM, Assaf EM. Syngas production via methane tri-reforming on Ni/La2O3–αAl2O3 catalysts. Braz J Chem Eng 2023;41:851–63. https://doi.org/10.1007/s43153-023-00352-9.

[14] Ho PH, de Nolf W, Ospitali F, Gondolini A, Fornasari G, Scavetta E, et al. Coprecipitated-like hydrotalcite-derived coatings on open-cell metallic foams by electrodeposition: rh nanoparticles on oxide layers stable under harsh reaction conditions. Appl Catal Gen 2018;560:12–20. https://doi.org/10.1016/j.apcata.2018.04.014.

[15] Gondolini A, Fasolini A, Mercadelli E, Basile F, Sanson A. Freeze cast porous membrane catalyst for hydrogen production via oxy-reforming. Fuel Process Technol 2021;213:106658. https://doi.org/10.1016/j.fuproc.2020.106658.

[16] Veiga S, Romero M, Bussi J. Facile deposition of a ni–la–zr catalyst on a FeCrAl monolith using the polymerized complex method: application to syngas production by tri-reforming of biogas. React Kinet Mech Catal 2024;137:1951–66. https://doi.org/10.1007/s11144-024-02631-z.

[17] Pandey A, Biswas P. Tri-reforming of methane over Ni/ZrO2 catalyst derived from Zr-MOF for the production of synthesis gas. Environ Sci Pollut Control Ser 2024;31:35069–82. https://doi.org/10.1007/s11356-024-33549-7.

[18] Son Phan T, Pham Minh D. Tri-reforming of methane over a hydroxyapatite supported nickel catalyst. ChemCatChem 2024;16. https://doi.org/10.1002/cctc.202400192.

[19] Tarifa P, Schiaroli N, Ho PH, Cañaza F, Ospitali F, Sanghez de Luna G, et al. Steam reforming of clean biogas over Rh and Ru open-cell metallic foam structured catalysts. Catal Today 2022;383:74–83. https://doi.org/10.1016/j.cattod.2021.03.024.

[20] Makhania M, Upadhyayula S. Foam: imparting structure to heterogeneous catalysis. ChemBioEng Rev 2022;9:591–604. https://doi.org/10.1002/cben.202200007.

[21] Zhang HK, Yin YR, Pan XQ, Zhang XM, Chen WX, Hu GH. The normal force evolution of the substrate during the withdrawal process. Polym Eng Sci 2022;62:3241–53. https://doi.org/10.1002/pen.26099.

[22] Niazmand M, Maghsoudipour A, Alizadeh M, Khakpour Z, Kariminejad A. Effect of dip coating parameters on microstructure and thickness of 8YSZ electrolyte coated on NiO-YSZ by sol-gel process for SOFCs applications. Ceram Int 2022;48:16091–8. https://doi.org/10.1016/j.ceramint.2022.02.155.

[23] Zuo C, Wang X, Ding X, Zhong Z, Jin W, Xing W. Combining dip-coating and rotate-drying to preparation of PDMS on SiC tubular support with macropore for high pervaporation performance. J Memb Sci 2024;705:122908. https://doi.org/10.1016/j.memsci.2024.122908.

[24] Prioriello A, Duranti L, Luisetto I, Sanna F, Larosa C, Grilli ML, et al. Structured catalyst for Indirect internal reforming (IIR) of biogas in solid oxide fuel cell (SOFC). Catalysts 2023;13. https://doi.org/10.3390/catal13071129.

[25] Santoro M, Luisetto I, Tuti S, Licoccia S, Romano C, Notargiacomo A, et al. Nickel-based structured catalysts for indirect internal reforming of methane. Applied Sciences (Switzerland) 2020;10. https://doi.org/10.3390/app10093083.

[26] Basile F, Benito P, Fornasari G, Monti M, Scavetta E, Tonelli D, et al. A novel electrochemical route for the catalytic coating of metallic supports, 175. Elsevier Masson SAS; 2010. https://doi.org/10.1016/S0167-2991(10)75007-2.

[27] Benito P, Monti M, De Nolf W, Nuyts G, Janssen G, Fornasari G, et al. Improvement in the coating homogeneity in electrosynthesized Rh structured catalysts for the partial oxidation of methane. Catal Today 2015;246:154–64. https://doi.org/10.1016/j.cattod.2014.10.003.

[28] Monti M, Benito P, Basile F, Fornasari G, Gazzano M, Scavetta E, et al. Electrosynthesis of Ni/Al and Mg/Al layered double hydroxides on Pt and FeCrAlloy supports: study and control of the pH near the electrode surface. Electrochim Acta 2013;108:596–604. https://doi.org/10.1016/j.electacta.2013.06.143.

[29] Benito P, De Nolf W, Nuyts G, Monti M, Fornasari G, Basile F, et al. Role of coating-metallic support interaction in the properties of electrosynthesized Rh-based structured catalysts. ACS Catal 2014;4:3779–90. https://doi.org/10.1021/cs501079k.

[30] Basile F, Benito P, Fornasari G, Monti M, Scavetta E, Tonelli D, et al. Novel Rh-based structured catalysts for the catalytic partial oxidation of methane. Catal Today 2010;157:183–90. https://doi.org/10.1016/j.cattod.2010.04.039.

[31] Varvoutis G, Lampropoulos A, Oikonomou P, Andreouli CD, Stathopoulos V, Lykaki M, et al. Fabrication of highly active and stable Ni/CeO2-nanorods wash-coated on ceramic NZP structured catalysts for scaled-up CO2 methanation. J CO2 Util 2023;70:102425. https://doi.org/10.1016/j.jcou.2023.102425.

[32] Kumar R, Pant KK. Promotional effects of Cu and Zn in hydrotalcite-derived methane tri-reforming catalyst. Appl Surf Sci 2020;515:146010. https://doi.org/10.1016/j.apsusc.2020.146010.

[33] Swirk Da Costa K, Grams J, Motak M, Da Costa P, Grzybek T. Understanding of tri-reforming of methane over ni/Mg/Al hydrotalcite-derived catalyst for CO2utilization from flue gases from natural gas-fired power plants. J CO2 Util 2020;42:1–7. https://doi.org/10.1016/j.jcou.2020.101317.

[34] Solov'ev SA, Gubareni YV, Kurilets YP, Orlik SN. Tri-reforming of methane on structured Ni-containing catalysts. Theor Exp Chem 2012;48:199–205. https://doi.org/10.1007/s11237-012-9262-x.

[35] Moncada Quintero CW, Mazzei HG, Servel M, Augier F, Haroun Y, Joly JF, et al. Investigating mass transfer coefficients in lean methane combustion reaction through the morphological and geometric analysis of structured open cell foam catalysts. Chem Eng Sci 2023;281. https://doi.org/10.1016/j.ces.2023.119138.

[36] Qi G, Li M, Chen R, Wang H, Wen H, Ding Y, et al. Development and optimization of gradient pore structured porous ceramics: modeling, properties, and potential for industrial production in thermal insulation engineering. Constr Build Mater 2025;486. https://doi.org/10.1016/j.conbuildmat.2025.142017.

[37] Ho PH, De Nolf W, Ospitali F, Beton D, Torkuhl L, Fornasari G, et al. Insights into coated NiCrAl open-cell foams for the catalytic partial oxidation of CH4. React Chem Eng 2019;4:1768–78. https://doi.org/10.1039/c9re00178f.

[38] Fasolini A, Spennati E, Ebrahim Atakoohi S, Percivale M, Busca G, Basile F, et al. A study of CO2 hydrogenation over Ni-MgAlOx catalysts derived from hydrotalcite precursors. Catal Today 2023;423:114271. https://doi.org/10.1016/j.cattod.2023.114271.

[39] Basile F, Fornasari G, Poluzzi E, Vaccari A. Catalytic partial oxidation and CO2-reforming on Rh- and Ni-based catalysts obtained from hydrotalcite-type precursors. Appl Clay Sci 1998;13:329–45. https://doi.org/10.1016/S0169-1317(98)00031-3.

[40] Fasolini A, Sangiorgi N, Tosi Brandi E, Sangiorgi A, Mariani F, Scavetta E, et al. Increased efficiency and stability of dye-sensitized solar cells (DSSC) photoanode by intercalation of eosin Y into Zn/Al layered double hydroxide. Appl Clay Sci 2021;212:106219. https://doi.org/10.1016/j.clay.2021.106219.

[41] Orfei E, Fasolini A, Abate S, Dimitratos N, Basile F. Layered-double hydroxides and derived oxide as CRM-free highly active catalysts for the reduction of 4-

nitrophenol. Catal Today 2023;419:114153. https://doi.org/10.1016/j.cattod.2023.114153.
[42] Gondolini A, Mercadelli E, Sangiorgi A, Sanson A. Integration of Ni-GDC layer on a NiCrAl metal foam for SOFC application. J Eur Ceram Soc 2017;37:1023–30. https://doi.org/10.1016/j.jeurceramsoc.2016.09.021.
[43] Gondolini A, Mercadelli E, Casadio S, Sanson A. Freeze cast support for hydrogen separation membrane. J Eur Ceram Soc 2022;42:1053–60. https://doi.org/10.1016/j.jeurceramsoc.2021.10.063.
[44] Gondolini A, Sangiorgi N, Sangiorgi A, Sanson A. Photoelectrochemical hydrogen production by screen-printed copper oxide electrodes. Energies 2021;14. https://doi.org/10.3390/en14102942.
[45] Bartoletti A, Gondolini A, Sangiorgi N, Aramini M, Ardit M, Rancan M, et al. Identification of structural changes in CaCu3Ti4O12 on high energy ball milling and their effect on photocatalytic performance. Catal Sci Technol 2022;13:1041–58. https://doi.org/10.1039/d2cy01299e.
[46] Almeida LC, Echave FJ, Sanz O, Centeno MA, Odriozola JA, Montes M. Washcoating of metallic monoliths and microchannel reactors, 175. Elsevier Masson SAS; 2010. https://doi.org/10.1016/S0167-2991(10)75004-7.
[47] Brinker CJ, Frye GC, Hurd AJ, Ashley CS. Fundamentals of sol-gel dip coating. Thin Solid Films 1991;201:97–108. https://doi.org/10.1016/0040-6090(91)90158-T.
[48] Carnicer V, Alcázar C, Orts MJ, Sánchez E, Moreno R. Microfluidic rheology: a new approach to measure viscosity of ceramic suspensions at extremely high shear rates. Open Ceramics 2021;5. https://doi.org/10.1016/j.oceram.2020.100052.
[49] Ebnesajjad S, Landrock AH. Adhesive applications and bonding processes. Adhesives Technology Handbook 2015;424:206–34. https://doi.org/10.1016/b978-0-323-35595-7.00008-5.
[50] Ballarini A, Benito P, Fornasari G, Scelza O, Vaccari A. Role of the composition and preparation method in the activity of hydrotalcite-derived Ru catalysts in the catalytic partial oxidation of methane. Int J Hydrogen Energy 2013;38:15128–39. https://doi.org/10.1016/j.ijhydene.2013.08.135.
[51] Takehira K, Shishido T. Preparation of supported metal catalysts starting from hydrotalcites as the precursors and their improvements by adopting "memory effect.". Catal Surv Asia 2007;11:1–30. https://doi.org/10.1007/s10563-007-9016-2.
[52] Tsyganok AI, Inaba M, Tsunoda T, Suzuki K, Takehira K, Hayakawa T. Combined partial oxidation and dry reforming of methane to synthesis gas over noble metals supported on Mg-Al mixed oxide. Appl Catal Gen 2004;275:149–55. https://doi.org/10.1016/j.apcata.2004.07.030.
[53] Balzarotti R, Ambrosetti M, Beretta A, Groppi G, Tronconi E. Investigation of packed conductive foams as a novel reactor configuration for methane steam reforming. Chem Eng J 2020;391:123494. https://doi.org/10.1016/j.cej.2019.123494.
[54] Zhang Y, Zhang S, Gossage JL, Lou HH, Benson TJ. Thermodynamic analyses of tri-reforming reactions to produce syngas. Energy Fuels 2014;28:2717–26. https://doi.org/10.1021/ef500084m.
[55] Izquierdo U, Barrio VL, Requies J, Cambra JF, Güemez MB, Arias PL. Tri-reforming: a new biogas process for synthesis gas and hydrogen production. Int J Hydrogen Energy 2013;38:7623–31. https://doi.org/10.1016/j.ijhydene.2012.09.107.
[56] Basile F, Basini L, D'Amore M, Fornasari G, Guarinoni A, Matteuzzi D, et al. Ni/mg/Al anionic clay derived catalysts for the catalytic partial oxidation of methane: residence time dependence of the reactivity features. J Catal 1998;173:247–56. https://doi.org/10.1006/jcat.1997.1942.
[57] Basile F, Benito P, Bugani S, De Nolf W, Fornasari G, Janssens K, et al. Combined use of synchrotron-radiation-based imaging techniques for the characterization of structured catalysts. Adv Funct Mater 2010;20:4117–26. https://doi.org/10.1002/adfm.201001004.
[58] Gazzano M, Kagunya W, Matteuzzi D, Vaccari A. Neutron diffraction studies of polycrystalline Ni/Mg/Al mixed oxides obtained from hydrotalcite-like precursors. J Phys Chem B 1997;101:4514–9. https://doi.org/10.1021/jp963761q.